

RESEARCH ARTICLE SUMMARY

ION CHANNELS

Structure of the human voltage-gated sodium channel $\text{Na}_v1.4$ in complex with $\beta 1$

Xiaojing Pan*, Zhangqiang Li*, Qiang Zhou*, Huaizong Shen*, Kun Wu*, Xiaoshuang Huang, Jiaofeng Chen, Juanrong Zhang, Xuechen Zhu, Jianlin Lei, Wei Xiong, Haipeng Gong, Bailong Xiao, Nieng Yan†

INTRODUCTION: The nine subtypes of mammalian voltage-gated sodium (Na_v) channels, $\text{Na}_v1.1$ to $\text{Na}_v1.9$, are responsible for the initiation and propagation of action potentials in specific excitable systems, among which $\text{Na}_v1.4$ functions in skeletal muscle. Responding to membrane potential changes, Na_v channels undergo sophisticated conformational shifts that lead to transitions between resting, activated, and inactivated states. Defects in Na_v channels are associated with a variety of neurological, cardiovascular, muscular, and psychiatric disorders. In addition, Na_v channels are targets for natural toxins and clinical therapeutics.

Understanding the physiological and pathophysiological mechanisms of Na_v channels requires knowing the structure of each conformational state. All eukaryotic Na_v channels comprise a single polypeptide chain, the α sub-

unit, that folds to four homologous repeats I to IV. Channel properties are modulated by one or two subtype-specific β subunits. Cryo-electron microscopy (cryo-EM) structures of two Na_v channels, one from American cockroach and the other from electric eel, were resolved in two distinct conformations. However, the inability to record currents of either channel in heterologous systems prevented functional assignment of these structures. Structural elucidation of a functionally well-characterized Na_v channel is required to establish a model for structure-function relationship studies.

RATIONALE: After extensive screening for expression systems, protein boundaries, chimeras, affinity tags, and combination with subtype-specific β subunits, we focused on human $\text{Na}_v1.4$ in the presence of $\beta 1$ subunit for cryo-EM analysis. The complex, which was

transiently coexpressed in human embryonic kidney (HEK) 293F cells with BacMam viruses and purified through tandem affinity columns and size exclusion chromatography, was concentrated to ~0.5 mg/ml for cryo-EM sample preparation and data acquisition.

RESULTS: The cryo-EM structure of human $\text{Na}_v1.4\text{-}\beta 1$ complex was determined to 3.2- \AA resolution. The extracellular and transmembrane domains, including the complete pore domain, all four voltage-sensing domains (VSDs), and the $\beta 1$ subunit, were clearly resolved, enabling accurate model building (see the figure).

ON OUR WEBSITE
Read the full article
at <http://dx.doi.org/10.1126/science.aau2486>

The well-resolved Asp/Glu/Lys/Ala (DEKA) residues, which are responsible for specific Na^+ permeation through the selectivity filter, exhibit identical conformations

to those seen in the other two Na_v structures. A glyco-diosgenin (GDN) molecule, the primary detergent used for protein purification and cryo-EM sample preparation, penetrates the intracellular gate of the pore domain, holding it open to a diameter of ~5.6 \AA . The central cavity of the pore domain is filled with lipid-like densities, which traverse the side wall fenestrations.

Voltage sensing involves four to six Arg/Lys residues on helix S4 of the VSD. This helix moves “up” (away from the cytoplasm) in response to changes of the membrane potential, and this opens the channel finally. All four VSDs display up conformations. The movement of the gating charge residues is facilitated by coordination to acidic and polar residues on S1 to S3. The improved resolution allows detailed analysis of the coordination.

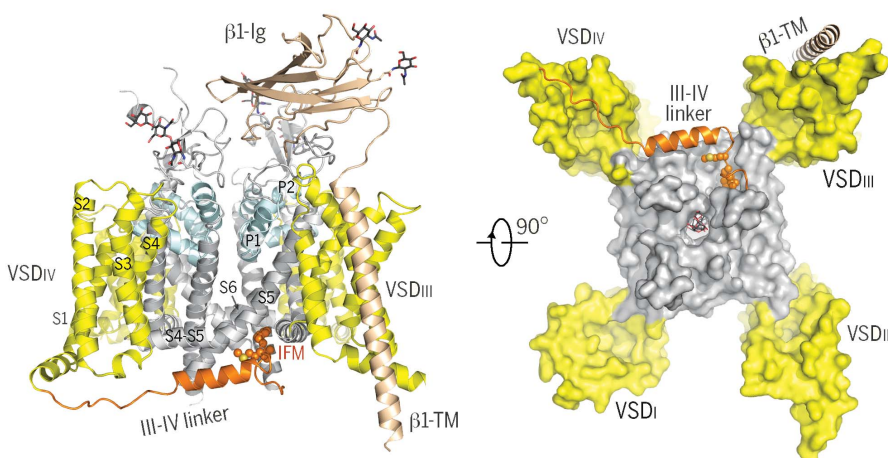
The fast inactivation Ile/Phe/Met (IFM) motif on the short linker between repeats III and IV inserts into a hydrophobic cavity enclosed by the S6 and S4-S5 segments in repeats III and IV. Analysis of reported functional residues and disease mutations corroborates our recently proposed allosteric blocking mechanism for fast inactivation.

CONCLUSION: The structure provides important insight into the molecular basis for Na^+ permeation, electromechanical coupling, asynchronous activation, and fast inactivation of the four repeats. It opens a new chapter for studying the structure-function relationships of Na_v channels, affords an accurate template to map mutations associated with diseases such as myotonia and periodic paralysis hyperkalemic, and illuminates a path toward precise understanding and intervention with specific Na_v channelopathies. ■

The list of author affiliations is available in the full article online.

*These authors contributed equally to this work.

†Corresponding author. Email: nyan@princeton.edu
Cite this article as X. Pan et al., *Science* **362**, eaau2486 (2018). DOI: [10.1126/science.aau2486](https://doi.org/10.1126/science.aau2486)



Structure of the human $\text{Na}_v1.4\text{-}\beta 1$ complex. Two perpendicular views are shown. Left: Side view in ribbon cartoon. The VSDs are colored yellow, and the selectivity filter and supporting helices P1 and P2 are colored light cyan. The IFM motif is shown as spheres, and the III-IV linker is colored orange. The transmembrane segments in repeat IV are labeled. Right: Surface presentation for the bottom view to highlight the intracellular gate and the cavity that accommodates the IFM motif. The GDN molecule that penetrates the intracellular gate is shown as thin sticks.

RESEARCH ARTICLE

ION CHANNELS

Structure of the human voltage-gated sodium channel $\text{Na}_v1.4$ in complex with $\beta 1$

Xiaojing Pan^{1,2,3,4*}, Zhangqiang Li^{1,2,3,5*}, Qiang Zhou^{1,2,4*}, Huaizong Shen^{1,2,4*}, Kun Wu^{3,6*}, Xiaoshuang Huang^{1,2,5}, Jiaofeng Chen^{3,5}, Juanrong Zhang^{2,3,5}, Xuechen Zhu⁵, Jianlin Lei^{5,7}, Wei Xiong^{3,5}, Haipeng Gong², Bailong Xiao^{3,6}, Nieng Yan^{1,2,3,5†‡}

Voltage-gated sodium (Na_v) channels, which are responsible for action potential generation, are implicated in many human diseases. Despite decades of rigorous characterization, the lack of a structure of any human Na_v channel has hampered mechanistic understanding. Here, we report the cryo-electron microscopy structure of the human $\text{Na}_v1.4-\beta 1$ complex at 3.2-Å resolution. Accurate model building was made for the pore domain, the voltage-sensing domains, and the $\beta 1$ subunit, providing insight into the molecular basis for Na^+ permeation and kinetic asymmetry of the four repeats. Structural analysis of reported functional residues and disease mutations corroborates an allosteric blocking mechanism for fast inactivation of Na_v channels. The structure provides a path toward mechanistic investigation of Na_v channels and drug discovery for Na_v channelopathies.

The physiological significance of voltage-gated sodium (Na_v) channels is underscored by their primary function in governing membrane excitability (1–5). More than 1000 point mutations have been identified in human Na_v channels associated with neurological, cardiovascular, muscular, and psychiatric disorders such as epilepsy, arrhythmia, muscle paralysis, pain syndrome, and autism spectrum disorder (6–9). Na_v channels represent major targets for a variety of natural toxins and clinical therapeutics (10–12).

In human, there are nine subtypes of Na_v channels, $\text{Na}_v1.1$ to $\text{Na}_v1.9$ (fig. S1) (13). $\text{Na}_v1.1$, $\text{Na}_v1.2$, $\text{Na}_v1.3$, and $\text{Na}_v1.6$ primarily function in the central nervous system. $\text{Na}_v1.4$ and $\text{Na}_v1.5$ work in skeletal muscle and heart, respectively, and $\text{Na}_v1.7$, $\text{Na}_v1.8$, and $\text{Na}_v1.9$ are mainly found in the peripheral nervous system. The ion-conducting core subunits (α subunits) are sufficient for voltage-dependent ion permeation; however, membrane trafficking and channel prop-

erties are modulated by one or two β subunits among four subtypes, $\beta 1$ to $\beta 4$ (14).

Na_v channels belong to the voltage-gated ion channel (VGIC) superfamily (15). Unlike most VGIC members that are homotetramers, eukaryotic Na_v channels comprise a single polypeptide chain of about 2000 residues that folds to four homologous but nonidentical repeats (repeats I to IV) (16). Each repeat contains six transmembrane segments (S1 to S6), among which S1 to S4 constitute the voltage-sensing domain (VSD), S5 and S6 from the four repeats together enclose the pore domain, and the sequences between S5 and S6 form the extracellular domains, the selectivity filter (SF), and the SF-supporting helices P1 and P2. Compared to Ca_v and K_v channels, Na_v channels have a highly asymmetric SF. Four distinct residues, Asp/Glu/Lys/Ala (DEKA), at corresponding locus in the SF of each repeat confer Na^+ selectivity (fig. S1) (17, 18).

A simplified diagram of the working cycle of Na_v channels is featured with transitions between resting, activated, and inactivated states (19). VSDs undergo conformational shifts in response to membrane potential changes, leading to the opening and closing of the pore domain (20, 21). Repetitively occurring basic residues Arg/Lys on the S4 segment, which represent the molecular basis for “gating charges” (GCs), are responsible for voltage sensing (16, 22, 23). At resting potential, the GC residues are attracted to the cytoplasmic side, and the pore domain is closed. Upon membrane depolarization, the outward movement of GC results in pore opening through a process known as electromechanical coupling (24).

Upon activation, Na_v channels immediately undergo fast inactivation, a critical mechanism that ensures recurring generation of action potentials. Decades of characterization have established the III-IV linker to be a key element for fast inactivation. The hydrophobic cluster Ile/Phe/Met (IFM) at the N terminus of the III-IV linker was defined as the fast inactivation motif (25–29). The binding site for the inactivation motif was less well understood, except that mutations on the S4-S5 linkers and S6 segments in repeats III and IV led to altered kinetics of fast inactivation (30, 31).

Understanding the physiological and pathophysiological mechanism of Na_v channels requires structural elucidation of a channel in multiple functional states. In contrast to their foundational status in modern biophysics, the structural study of eukaryotic Na_v channels lagged behind other VGIC members (32–35). The pseudosymmetry, heavy posttranslational modifications, and medium molecular weight make Na_v channels one of the most challenging targets for both x-ray crystallography and electron cryo-electron microscopy (cryo-EM) analyses.

The eukaryotic Na_v channels were structurally unveiled in 2017. The cryo-EM structures of Na_vPaS , a subtype from American cockroach, and $\text{EeNa}_v1.4$, a prototypal Na_v channel from electric eel, were determined to resolutions of 3.8 and 4.0 Å, respectively, in different conformations (36, 37). In the structure of Na_vPaS , the intracellular gate is tightly closed and the side walls are sealed without fenestrations, reminiscent of what is expected for the resting state. However, the VSDs exhibit “up” conformations but are distinct from fully activated conformations. Meanwhile, the III-IV linker is sequestered by the globular C-terminal domain (CTD), unlikely to be able to execute its inactivating function. In contrast, the structure of $\text{EeNa}_v1.4$ exhibits the following features. (i) The intracellular gate is held unsealed by a digitonin-like molecule. (ii) Whereas side groups could not be assigned for VSDs in repeats I and II, the well-resolved VSD_{III} and VSD_{IV} are both up. (iii) The IFM motif is positioned in the corner enclosed by the S6 segments and the S4-S5 linkers in repeats III and IV.

Despite the conformational distinctions, functional states cannot be defined for the two structures in the absence of other reference structures. In addition, the inability to record Na_vPaS and $\text{EeNa}_v1.4$ channel currents in heterologous systems prevents functional characterization of the structures. Therefore, structural determination of a functionally well-characterized Na_v channel is required to establish a model for structure-function relationship studies.

Results

Protein generation and structural determination of the human $\text{Na}_v1.4-\beta 1$ complex

The bottleneck for cryo-EM analysis of any human Na_v channel is the production of well-behaved recombinant proteins and preparation

¹State Key Laboratory of Membrane Biology, Tsinghua University, Beijing 100084, China. ²Beijing Advanced Innovation Center for Structural Biology, Tsinghua University, Beijing 100084, China. ³Tsinghua-Peking Joint Center for Life Sciences, Tsinghua University, Beijing 100084, China.

⁴School of Medicine, Tsinghua University, Beijing 100084, China. ⁵School of Life Sciences, Tsinghua University, Beijing 100084, China. ⁶School of Pharmaceutical Sciences, Tsinghua University, Beijing 100084, China. ⁷Technology Center for Protein Sciences, Ministry of Education Key Laboratory of Protein Sciences, Tsinghua University, Beijing 100084, China.

*These authors contributed equally to this work.

†Present address: Department of Molecular Biology, Princeton University, Princeton, NJ 08544, USA.
‡Corresponding author. Email: nyan@princeton.edu

of cryo-samples. We have exploited different eukaryotic expression systems for all nine subtypes of human Na_v channels and screened a variety of boundaries, internal truncations, chimeras, affinity tags, and combination with β subunits (38). The expression level of $\text{Na}_v1.4$, a functionally well-defined subtype (39–41), was higher than that of the other isoforms. $\text{Na}_v1.4$ has been extensively investigated with multiple biophysical approaches for functional and mechanistic characterization (42–46). We therefore focused on $\text{Na}_v1.4$ for further optimization of protein production and purification.

The channel properties of the overexpressed human $\text{Na}_v1.4$, with or without the subtype-specific $\beta 1$ subunit, are consistent with previous reports (fig. S2) (47, 48). When coexpressed with the human $\beta 1$ subunit, ~20 to 30 μg of purified protein can be obtained from 12 liters of human embryonic kidney (HEK) 293F cells by transient plasmid expression. The expression level was doubled when BacMam viruses were used to transiently coexpress the complex in HEK293F cells (49). The protein behaved relatively well upon size exclusion chromatography (Fig. 1A).

Although the preliminary negative staining EM analysis showed intact particles, the proteins were prone to aggregation under cryo-conditions. After another round of systematic screening, we obtained optimal cryo-samples. Details of the purification are in Materials and methods. Briefly, the full-length wild-type human $\text{Na}_v1.4$ was tandemly tagged with twin strep and FLAG on the N terminus. The $\text{Na}_v1.4-\beta 1$ complex was extracted using 1% (w/v) n -dodecyl- β -D-maltopyranoside supplemented with 0.2% (w/v) cholesteryl hemisuccinate and subsequently purified in the presence of 0.06% (w/v) glycodeosigenin (GDN; Anatrace). After tandem affinity purification and size exclusion chromatography, the presence of the complex was confirmed by mass spectrometric analysis.

Details of cryo-grid preparation, data acquisition, and structural determination can be found in Materials and methods. Out of ~1.7 million particles collected on a Titan Krios electron microscope equipped with Cs corrector, Gatan K2 Summit detector, and GIF Quantum energy filter, a total of 191,936 particles were selected to yield an EM map with the overall resolution of 3.2 Å according to the gold standard Fourier shell correlation (FSC) 0.143 criterion (Fig. 1, B to F; figs. S3 and S4; and table S1). Nearly all the extracellular and transmembrane sequences are well resolved except for residues 287 to 335, an extracellular segment between $S5_1$ and $S6_1$ (where “I” indicates repeat I) that is least conserved between $\text{Na}_v1.4$ and the other eight subtypes (fig. S1).

Overall structure of the $\text{Na}_v1.4-\beta 1$ complex

In total, 1311 side chains were built for the human $\text{Na}_v1.4-\beta 1$ complex (table S1). The overall structure is nearly identical to that of the Ee $\text{Na}_v1.4-\beta 1$ complex, with a root mean square deviation of 0.955 Å over 1111 Ca atoms. Even

the glycosylation sites completely overlap, highlighting the evolutionary conservation (fig. S5). Nevertheless, the markedly improved resolution enabled more accurate model building for detailed analysis of the functional entities such as the SF and all four VSDs (Fig. 2, A and B, and fig. S4). In addition, densities corresponding to four phospholipids are found attached to the pore domain. Three additional linear densities traverse the fenestrations on three sides of the pore domain and fill up the central cavity (Fig. 2A and fig. S6).

The common structural features between $\text{Na}_v1.4-\beta 1$ complexes from human and electric eel include the interactions between $\beta 1$ and $\text{Na}_v1.4$ (Fig. 2A and fig. S5), the acidic residue-enriched and multiple disulfide bond-stabilized extracellular loops above the pore domain (Fig. 2B), and a detergent molecule-penetrated intracellular gate (Fig. 2, C and D, and fig. S6A). This density, which can now be perfectly docked with a GDN molecule, is plugged into the intracellular

gate of $\text{Na}_v1.4$, holding the intracellular gate open to a radius of 2.8 Å, slightly wider than that in Ee $\text{Na}_v1.4$ (Fig. 2, C and D, and fig. S6B). Because these features have been illustrated in detail for Ee $\text{Na}_v1.4$ (37), we will not elaborate on them in this study. Instead, we will focus on the SF and the VSDs, which are now elucidated to near-atomic resolution.

The asymmetric SF

In Na_v channels, the sieve on the extracellular side for ion permeation, or the high-field strength site (50), consists of an outer negative ring constituted by Asp/Glu residues on the first turn of the P2 pore helix in each repeat, the signature DEKA motif, and a wide inner site enclosed by eight carbonyl oxygens (36). The DEKA motif (Asp⁴⁰⁶/Glu⁷⁶¹/Lys¹²⁴⁴/Ala¹⁵³⁶) was reliably resolved in the EM reconstruction for human $\text{Na}_v1.4$ with a local resolution of up to 2.8 Å (Figs. 1F and 3A).

The outer acidic residue Asp or Glu is separated from the corresponding locus of the DEKA

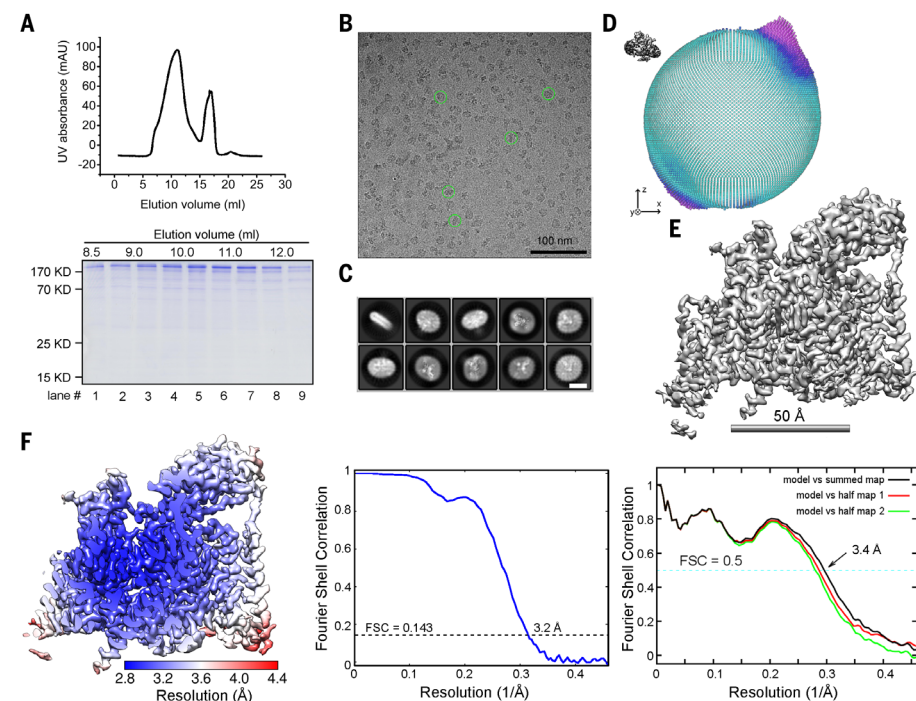


Fig. 1. Cryo-EM analysis of the human $\text{Na}_v1.4-\beta 1$ complex. (A) Last step purification of recombinantly expressed $\text{Na}_v1.4-\beta 1$ complex. A representative chromatogram of gel filtration purification is shown. The indicated fractions were resolved by SDS-polyacrylamide gel electrophoresis followed by Coomassie blue staining. The presence of $\beta 1$, although invisible on the gel, was confirmed by mass spectrometric analysis. (B) Representative electron micrograph of the $\text{Na}_v1.4-\beta 1$ complex. Characteristic particles in distinct orientations are highlighted by green circles. (C) Representative 2D class averages of $\text{Na}_v1.4-\beta 1$ particles. Scale bar, 10 nm. (D) Angular distribution of the final reconstruction. Each column represents one view, and the size of the column is proportional to the number of particles in that view. (E) EM map for the human $\text{Na}_v1.4-\beta 1$ complex. The map is generated in Chimera (83). (F) Overall resolution of 3.2 Å. Left: Local resolution map calculated with Relion 2.0. Middle: Gold standard FSC curve for the 3D reconstruction. Right: FSC curves of the refined model versus the overall 3.2 Å map that it was refined against (black), of the model refined in the first of the two independent maps used for the gold standard FSC versus that same map (red), and of the model refined in the first of the two independent maps versus the second independent map (green). The small difference between the red and green curves indicates that the refinement did not suffer from overfitting. UV, ultraviolet.

motif by two residues in repeats I, II, and IV, and three in repeat III. Yet, the SF segment in repeat II is one residue shorter than those in the other repeats, with the invariant Trp immediately following Glu instead of being separated by one residue (fig. S1). Consequently, Glu⁷⁶⁴ and Asp¹²⁴⁸ are aligned above E and K in repeats II and III, respectively, whereas Glu⁴⁰⁹ in repeat I and Asp¹⁵³⁹ in repeat IV are shifted aside by about 120° (Fig. 3B). This spatial arrangement creates additional asymmetry at the entrance to SF (Fig. 3, B and C). The carboxylate groups of Glu⁷⁶⁴ on P2_{II} and DE (Asp⁴⁰⁶/Glu⁷⁶¹ in hNa_v1.4) are clustered to constitute a highly electronegative site, which we referred to as the DEE site (Fig. 3C). A Na⁺ ion is coordinated by DEE in a 2.6-Å cryo-EM structure of Na_vPaS (57), but no density is observed inside or adjacent to the SF vestibule in the EM map for human Na_v1.4.

Nearly half a century ago, Hille suggested that the cross-section of the constriction in Na_v channels is about 3 Å by 5 Å (52), which can now be explained by the structure. The distance between

the amine of K (Lys¹²⁴⁴) on repeat III and the opposing carbonyl oxygen of D (Asp⁴⁰⁶) on repeat I is ~3.5 Å and marks the constriction point along the permeation path (Figs. 2D and 3D), whereas the distance of the corresponding loci on repeats II and IV is longer (Fig. 3D).

In our recent molecular dynamics (MD) simulation analysis of Na_vPaS, the side chains of DEE residues remain relatively rigid during Na⁺ penetration (53). The well-resolved local densities show that both Glu⁷⁶¹ and Glu⁷⁶⁴ are stabilized by the guanidinium group of an adjacent invariant Arg⁷⁵⁶ on the P2_{II} helix (Fig. 3D, left). The electronegative surface of the extracellular loops and the outer mouth to the SF vestibule can effectively attract cations and repel anions (Fig. 3E). Once cations are drawn to the outer vestibule of the SF, they are likely driven to the DEE site owing to electrostatic attraction (Fig. 3, C to E). The geometric arrangement of the three carboxylate groups of DEE and the dimension of the constriction site may collectively confer Na⁺ selectivity (53).

The four VSDs exhibit up conformations

The voltage-dependent movement of GC residues is facilitated by a number of conserved acidic and polar residues exemplified by two residues on S2 (designated An1 and An2) and one invariant Asp on S3 segments (54–57). An2 and a cyclic hydrophobic residue on S2 and the S3-Asp were functionally defined as the charge transfer center (CTC) (fig. S1) (58). Structure-based sequence alignment of the four VSDs in human Na_v1.4 shows that the corresponding segments of S2 to S4 in the four domains have different lengths (Fig. 4A). For instance, there are six helical turns in S4_I and S4_{II}, and seven in S4_{III} and S4_{IV}. The number of GC residues varies from four to six in the four VSDs (Fig. 4A). We defined the one on the last intracellular helical turn of S4 as the sixth GC (36, 37, 59). There are four GC residues (R2 to R4 and K5) in VSD_I, five (R2 to R4, K5, and K6) in VSD_{II}, five (K1 and R2 to R5) in VSD_{III}, and six (R1 to R5 and R/K6) in VSD_{IV}. In addition, an Arg is positioned four, instead of three, residues away from R5 in VSD_{III}

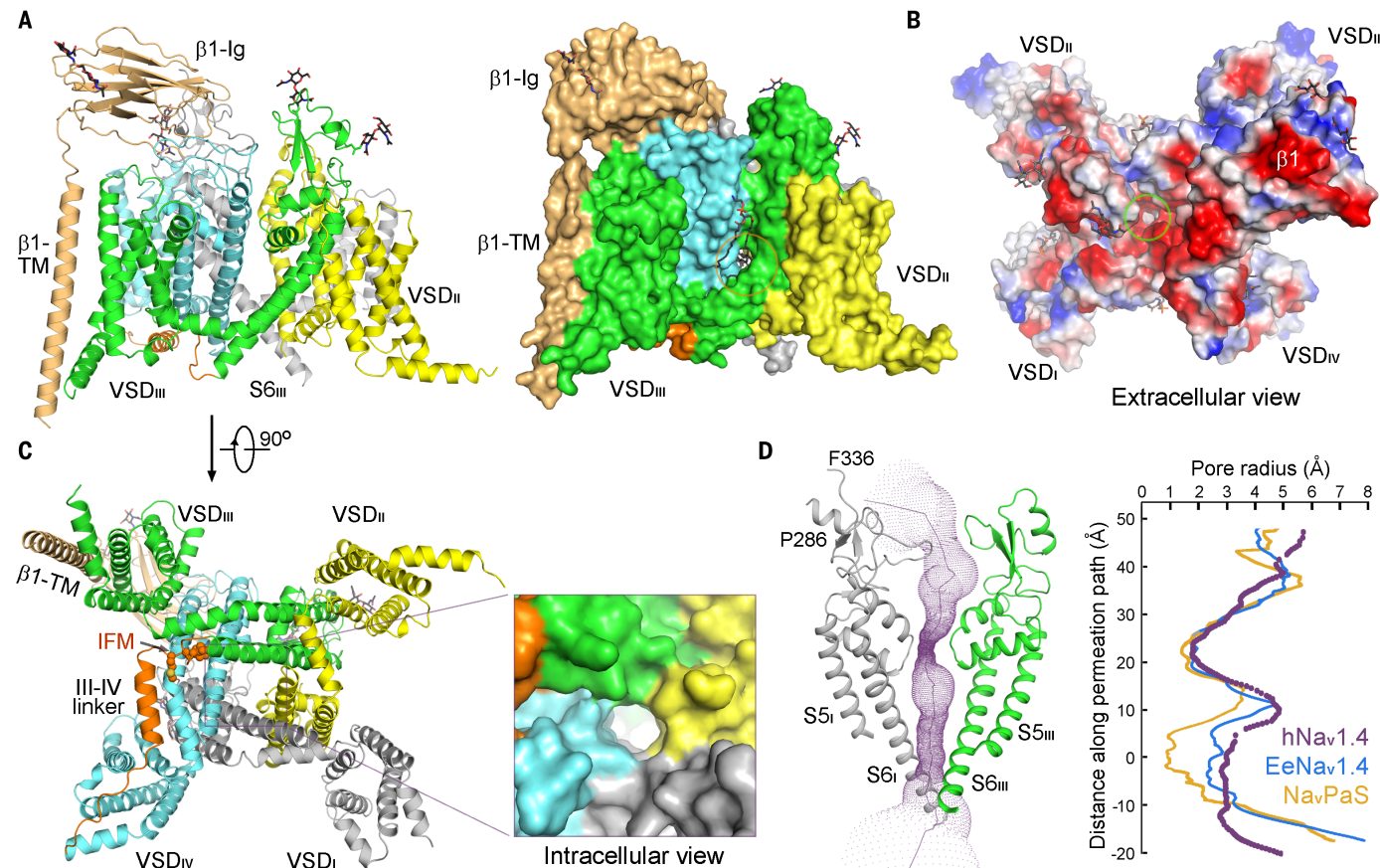


Fig. 2. Structure of the human Na_v1.4-β1 complex. (A) The extracellular and transmembrane regions of the Na_v1.4-β1 complex are clearly resolved. The structure is domain colored. The glycosyl moieties are shown as sticks. The same side view is shown in cartoon (left) and surface (right) representations. (B) The extracellular surface of the pore domain is highly electronegative. The surface electrostatic potential is calculated in PyMOL (87). (C) The intracellular gate of Na_v1.4 is kept unclosed. The IFM fast inactivation motif is shown as spheres, and the III-IV linker

is colored orange. Inset: Intracellular gate. Detailed analysis of the hydrophobic intracellular gate that is penetrated by a GDN molecule is presented in fig. S6B. (D) The SF marks the constriction site along the permeation path in the pore domain. The permeation path, calculated by HOLE (88), is illustrated by purple dots in the left panel. The corresponding pore radii of human Na_v1.4 (purple), EeNa_v1.4 (blue), and Na_vPaS (orange) are compared in the right panel. All structure figures were prepared in PyMOL. Ig, immunoglobulin.

of Na_v .1 to Na_v .1.8 (Fig. 4A and fig. S1). As the sequences of each corresponding VSD in the nine Na_v subtypes are highly conserved, the observed VSD structures in human Na_v .1.4 are likely shared by all mammalian Na_v channels (fig. S1).

In the present Na_v .1.4 structure, the S4 segment harboring R2 to R6 is a β_{10} helix in all four VSDs, while the R1-carrying segment is relaxed to an α helix in VSDs III and IV (Fig. 4B). When individual VSDs are superimposed relative to the CTC, the height of the Ca atoms of corresponding GCs is III > I > IV > II (Fig. 4B and fig. S7). In all four VSDs, GCs R/K1 to R4 are above the occluding aromatic Tyr/Phe on S2. R5 in I, II, and IV is below the occluding residue and coordinated by the acidic residues in CTC, whereas R5 in VSD_{III} is at a similar height to Phe¹⁰⁷⁶, forming π -cation interaction (Fig. 4C and fig. S7). In total, 15 amine or guanidinium groups in the four VSDs—3 each in VSD_I and VSD_{II}, 5 in VSD_{III}, and 4 in VSD_{IV}—are on the extracellular side of the occluding Phe/Tyr (Fig. 4C and fig. S7). Although the VSDs appear in different up conformations, their functional states cannot be defined in the absence of reference structures in other conformations, such as the resting state.

The improved resolution allows detailed analysis of the coordination of GCs in each VSD. The interactions between GCs and An1 and CTC are presented in detail in Fig. 4C and fig. S7 and will not be enumerated here. It is noteworthy that several conserved polar or acidic residues on the corresponding loci of S1, which have been less characterized before, also participate in the coordination of GCs (Fig. 4, A and C). In VSDs II to IV, an invariant Glu on the extracellular tip of S1 interacts with R2, while a polar residue in the middle of S1 (Ser in VSD_{III} and Asn in the other three VSDs) coordinates R4. On the intracellular tip of S1, an invariant Asp (Asp⁵⁸¹ in VSD_{II} and Asp¹³⁵⁶ in VSD_{IV}) interacts with K6/R6, and a Glu (Glu¹⁰³⁴) interacts with the C-terminal Arg¹¹⁴² in VSD_{III} (Fig. 4C). The intracellular locus on S1_I is occupied by Ser or Asn (Fig. 4A and fig. S1), which is not involved in the interaction with S4 residues in the present structure, but may participate in GC coordination in other functional states.

The varied numbers and chemical characteristics of GCs (Lys versus Arg) and charge transfer facilitating residues (D/E/N/S) will naturally result in distinct affinities between S4 and surrounding elements in different VSDs, thereby providing the molecular basis for asynchronous movements of the VSDs during voltage-dependent activation (42, 60). In addition, the distinct interface between each VSD and the pore domain further contributes to the functional asymmetry of the four repeats and adds to the complexity in dissecting the electromechanical coupling mechanism of Na_v channels (fig. S8) (42, 60).

Structural basis for fast inactivation

In the cryo-EM structures of Na_v PaS and Ca_v .1.1, the III-IV linker is both sequestered by the glob-

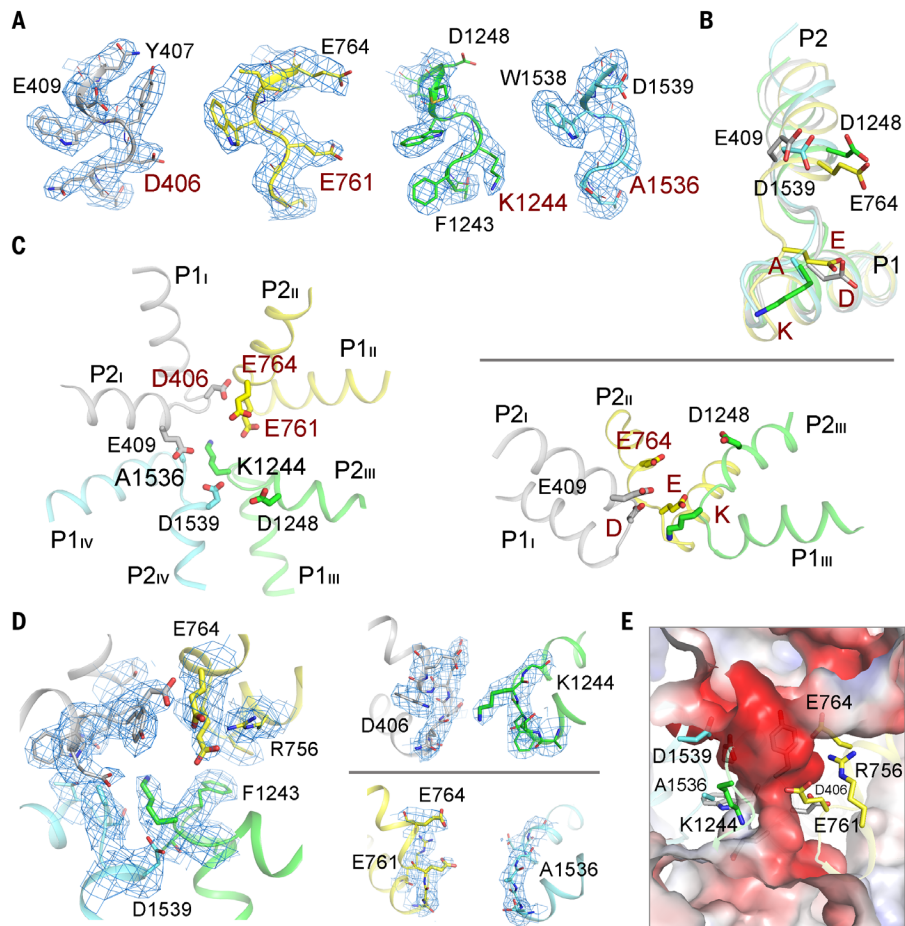


Fig. 3. The asymmetric SF. (A) All the residues that constitute the SF are well resolved in Na_v .1.4. The densities, shown as blue mesh, are contoured at 5σ . The signature DEKA residues are labeled dark red. (B) Superimposition of the P1-SF-P2 segments from the four repeats. DEKA motif and the residues that constitute the outer negative ring are shown as sticks. (C) Structure of the SF. A top view is shown on the left, and a side view with repeat IV omitted is shown on the right. Asp⁴⁰⁶ and Glu⁷⁶¹ in the DEKA motif and Glu⁷⁶⁴ on P2_{II} form a favorite Na^+ binding site, designated the DEE site, consistent with the observation in the structure and MD simulation of Na_v PaS (51, 53). (D) Asymmetric SF vestibule. The densities for the residues that constitute the SF vestibule are contoured at 5σ . An extracellular view (left) and two side views of diagonal repeats (right) are shown. (E) Potential Na^+ permeation path. A cut-open side view of the surface electrostatic potential of the SF vestibule is shown.

ular CTD (36, 59), offering a structural basis for the observed functional importance of the CTD in inactivation (61–63). However, neither Na_v PaS nor Ca_v .1 has the IFM motif. In the structure of Ee Na_v .1.4, the III-IV linker is repositioned relative to Na_v PaS and Ca_v .1, and the IFM motif is plugged into the corner between the S6 and the S4-S5 segments in repeats III and IV. On the basis of the conformational changes between Na_v PaS and Ee Na_v .1.4, we postulated an allosteric blocking mechanism wherein the IFM motif does not directly block the pore but pushes pore closure by squeezing into the space between the S6 helical bundle and the S4-S5 restriction ring (37). Nonetheless, the moderate resolution of the Ee Na_v .1.4 structure limited analysis of local interactions.

The IFM motif and surrounding residues were unambiguously resolved in human Na_v .1.4

(Fig. 5, A and B). Midway between the intracellular gate and VSD_{III}, the S4-S5 and S6 segments in repeats III and IV together with S5_{IV} enclose a hydrophobic cavity (Fig. 5A). The aromatic ring of Phe¹³¹¹ inserts deeply into the cavity, whereas Ile¹³¹⁰ and Met¹³¹² buttress the interaction by binding to the edges of the cavity (Fig. 5, A and B). This structural feature is consistent with mutagenesis of the IFM motif, which showed that the single point mutation of Phe to Gln had a more pronounced effect on fast inactivation than mutation of either Ile or Met (29).

The III-IV helix that follows the IFM motif interacts extensively with S4-S5_{IV} through van der Waals contacts (Fig. 5, C and D). Mutations of Phe¹⁴⁷³, Met¹⁴⁷⁶, and Met¹⁴⁷⁷ on S4-S5_{IV}, which are mapped to the interface with the III-IV linker, resulted in fast inactivation defects (64, 65). In

addition, Asn¹⁴⁸⁴ on S5_{IV} is hydrogen bonded to both the side group of Gln¹³¹⁶ on the first helical turn of the III-IV helix and the carbonyl oxygen of Phe¹³¹¹. Mutation of the corresponding Asn to Ala in rat Na_v1.2 completely abolished fast inactivation (65). Ala substitution or mutation of hydrophobic residues to polar residues would disrupt or weaken the association between the III-IV linker and the involved segments. Therefore, these mutagenesis characterizations provide strong support for the critical role of the structurally revealed interface in fast inactivation.

Structural analysis of disease mutations

Near-atomic resolution structures of human Na_v channels can provide accurate templates to analyze disease-related mutations (table S2), thereby illuminating a path toward precise understanding and intervention with specific Na_v chan-

nelopathies. More than 70 mutations have been identified in human Na_v1.4 associated with different forms of myotonia and periodic paralysis hyperkalemic (Fig. 6 and table S2). Structural mapping identified several hotspots for disease mutations, several of which are discussed below (Fig. 6).

GC residues represent important hotspots in all Na_v channels owing to their fundamental role in voltage sensing and electromechanical coupling (8). Only mutations of upper GC residues R1 to R4, but not R5 or R6 in Na_v1.4, are found in several types of disease (Fig. 6). Although GC-interacting residues also affect voltage-dependent movements of S4, only one disease mutation D1069N (An1 in VSD_{III}) was discovered (Fig. 6C).

Another hotspot is related to fast inactivation. Some pathogenic mutations were characterized

to cause inactivation defects, such as A1152D (66, 67), G1306→A/E/V (68, 69), and T1313M (70). Ala¹¹⁵² is a residue in the hydrophobic cavity and directly interacts with Ile¹³¹⁰ and Phe¹³¹¹ (Fig. 5B). Gly¹³⁰⁶ is located at the sharp turn between S6_{III} and the IFM motif. Substitution of Gly with side groups may alter the secondary structure. Thr¹³¹³ immediately follows the IFM motif. It contributes to the polar interaction between Gln¹³¹⁶ on the III-IV helix and Asn¹⁴⁸⁴ on S5_{IV} (Fig. 5, C and D). The mutation A1481D is responsible for cold-induced myotonia (71). Ala is mapped to S4-5_{IV}, in direct contact with both Phe¹³¹¹ and Met¹³¹² (Fig. 5, B and D). The structure thus provides a molecular interpretation for the inactivation defects, and these disease mutations, in turn, serve as evidence for the allosteric blocking mechanism suggested based on the structure (8).

Conclusions

Structural determination of an intact human Na_v channel to near-atomic resolution opens a new chapter for studying the structure-function relationships of these channels, which are of remarkable physiological and pathophysiological significance. The structure bridges the large body of experimental and clinical data accumulated in the past seven decades to future structure-based mechanistic investigations, drug discovery, and protein engineering. The methods for protein generation and data processing of human Na_v1.4 could also inform the cryo-EM structural analysis of other Na_v subtypes.

The transitions between voltage-dependent working states of Na_v channels entail complicated conformational changes and rearrangement of interactions between adjacent or even distant structural elements through direct or allosteric effects. It is impossible to fully interpret functional and mutational observations based on one structure. It is thus important to elucidate the structures of a specific channel in distinct functional states. In this regard, structural resolution of the functionally well-defined Na_v1.4 represents an exciting start point to eventually unveil the choreography of voltage-dependent electromechanical coupling of Na_v channels by means such as mutagenesis and ligand interference.

Materials and methods

Transient coexpression of human Na_v1.4 and β1

The optimized coding DNAs for human Na_v1.4 (Uniprot: P35499) and β1 (Uniprot: Q07699) were cloned into the pEG BacMam vector (49), with tandem twin Strep-tag and FLAG tag at the N terminus of Na_v1.4. The BacMam viruses were produced and amplified in Sf9 cells (Invitrogen). The HEK293F cells (Invitrogen) were cultured in SMM 293T-I medium (Sino Biological Inc.) supplemented with 5% CO₂ in a Multitron-Pro shaker (Infors, 130 r.p.m.) at 37°C. When cell density reached 4 × 10⁶ cells per ml, the culture was diluted to 2 × 10⁶ cells per ml with fresh medium and transfected with the P2 (the second

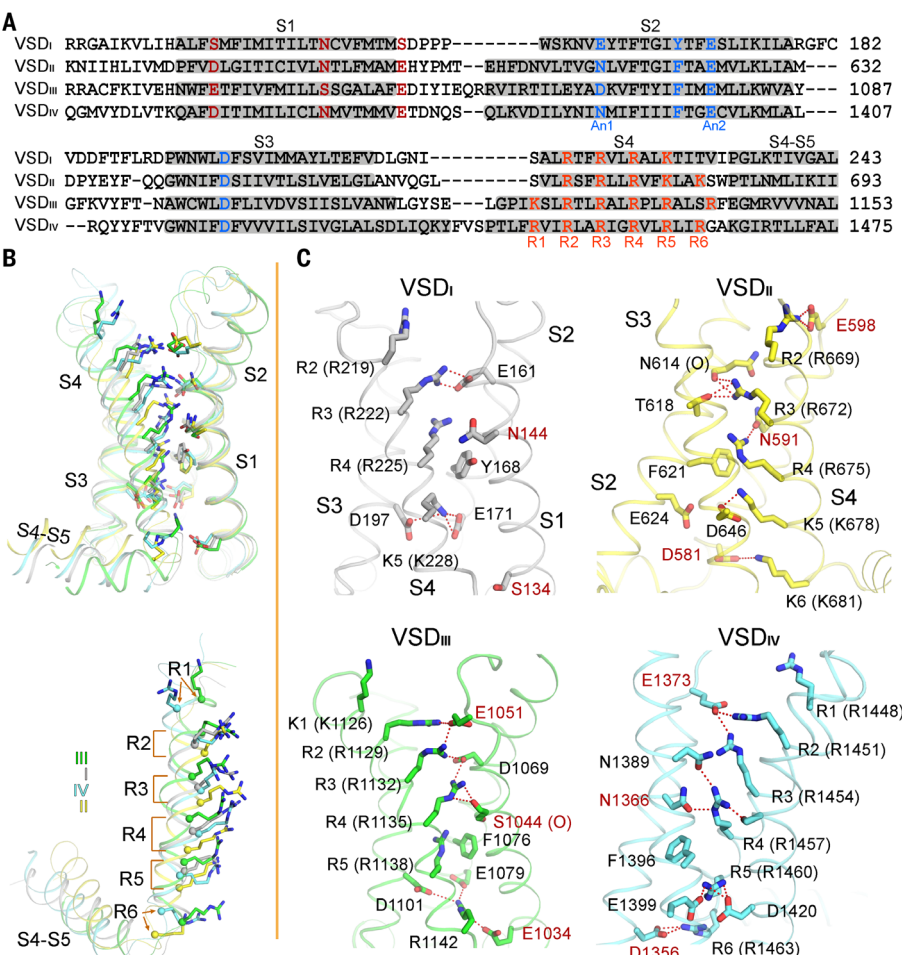


Fig. 4. Molecular basis for the functional asymmetry of the VSDs. (A) Structure-based sequence alignment of the four VSDs in human Na_v1.4. The VSDs are superimposed in PyMOL, and the resulting sequence alignment is shown. The CTC, GC residues, and the conserved polar or acidic residues on S1 that coordinate GCs are highlighted with blue or red colors. The boundaries for the S1 to S4 helices are shaded gray. (B) All four VSDs exhibit up conformations. Top: The four VSD structures are superimposed relative to CTC and An1 on S2. Bottom: The corresponding GC residues in the four VSDs are at different heights relative to the CTC. The Ca atoms of the GC residues are shown as spheres. (C) Distinct interior compositions of the four VSDs. The GC residues on S4 and their coordinating residues on S1 to S3 are shown as sticks. The electrostatic interactions are indicated by red dashed lines. The polar residues on S1 that may facilitate charge transfer are labeled red.

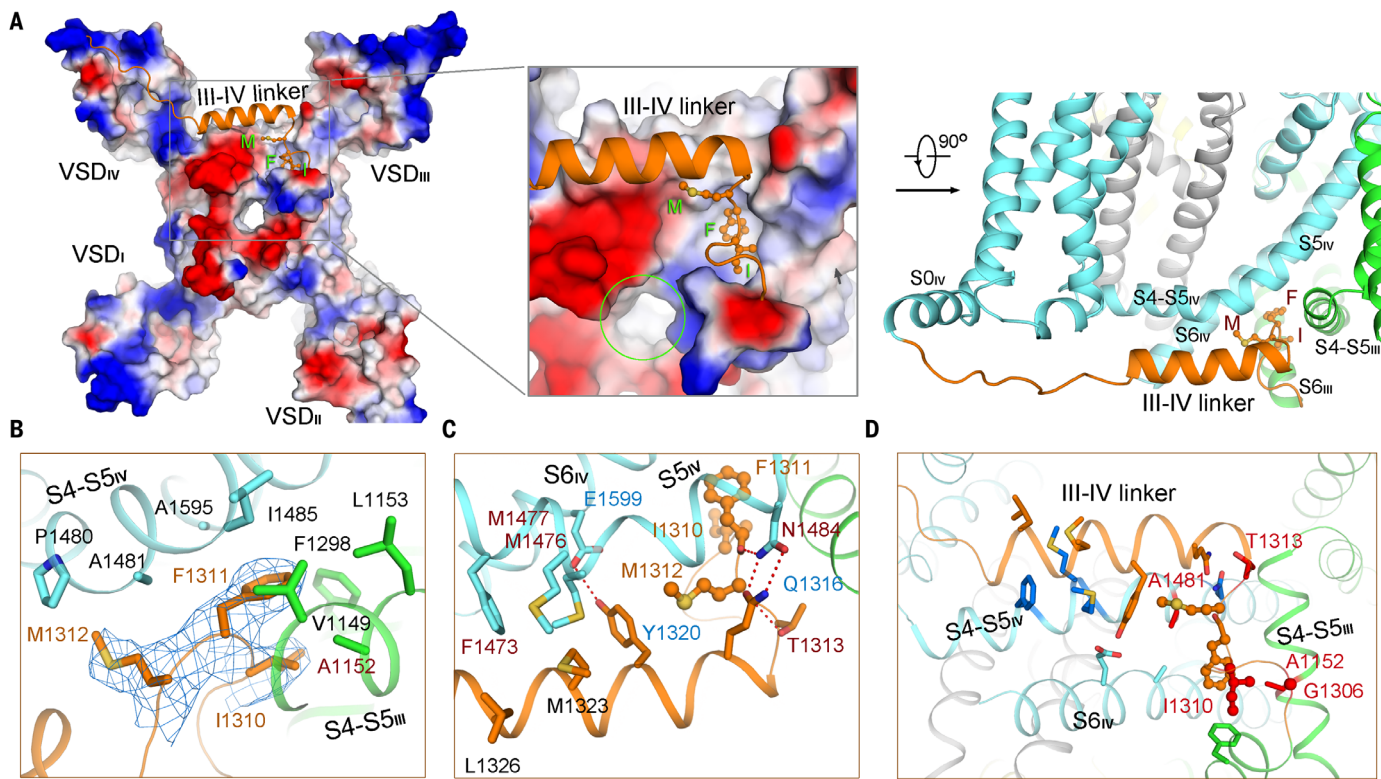


Fig. 5. An allosteric blocking mechanism for fast inactivation. (A) The fast inactivation IFM motif inserts into a hydrophobic cavity enclosed by the S4-S5 and S6 segments in repeats III and IV. An intracellular view of the electrostatic surface potential is shown to highlight the hydrophobic cavity. Inset: The intracellular gate is indicated by green circle. (B) Accommodation of the IFM motif. The density for the IFM motif, shown as blue mesh, is contoured at 5σ . (C) Extensive interactions between the III-IV motif and adjacent elements. The residues

that were previously identified to be important for fast inactivation and those involved in polar interactions are labeled brown and blue, respectively. (D) Structural analysis of disease mutations that cause fast inactivation defects. An intracellular view is shown. The residues whose mutations are found in various types of myotonia are colored and labeled red. The residues that were characterized to be involved in fast inactivation are colored blue. IFM residues are shown as ball and sticks.

passage) BacMam viruses of $\text{Na}_v1.4$ and $\beta 1$, each at 25 ml per liter cell culture. Sodium butyrate was added to the cell culture at a final concentration of 10 mM to facilitate protein expression. Transfected cells were cultured for 48 hours before harvesting.

Purification of the $\text{Na}_v1.4-\beta 1$ complex

For each batch of protein purification, 12 liters of transfected cells were harvested by centrifugation at 800 g and resuspended in lysis buffer containing 25 mM imidazole, pH 5.9, and 150 mM NaCl. The suspension was supplemented with 1% (w/v) *n*-dodecyl- β -D-maltopyranoside (DDM, Anatrace), 0.2% (w/v) cholestryl hemisuccinate Tris salt (CHS, Anatrace), 0.001% (w/v) dodecyl sulfate sodium salt (SDS, BIO-RAD), and protease inhibitor cocktail including 2 mM phenylmethylsulfonyl fluoride (PMSF), 6.5 μ g/ml aprotinin, 3.5 μ g/ml pepstatin, and 25 μ g/ml leupeptin. After incubation at 4°C for 3 hours, the solution was ultra-centrifuged at 200,000 g for 30 min, and the supernatant was applied to anti-Flag M2 affinity resin (Sigma) by gravity at 4°C. The resin was rinsed four times with the W buffer, which contains 25 mM imidazole pH 5.9, 150 mM NaCl, 0.06% (w/v) glyco-diosgenin

(GDN, Anatrace), 0.001% SDS, and the protease inhibitor cocktail. The target proteins were eluted with W buffer plus 200 μ g/ml FLAG peptide (Sigma). The eluent was then applied to Strep-Tactin Sepharose (IBA) and the purification protocol was similar to the previous step except that the elution buffer was W buffer plus 2.5 mM D-desthiobiotin (IBA). After incubation at 4°C overnight with addition of GDN to a final concentration of 0.12%, the eluent was then concentrated using a 100-kDa cut-off Centricon (Millipore) and further purified by Superose-6 column (GE Healthcare) also in the W buffer. The presence of the complex was confirmed by mass spectrometry.

Whole-cell electrophysiology

The DNAs of $\text{Na}_v1.4$ and $\beta 1$ were cloned into the pCAG vector (72). The HEK293T cells, which were cultured in Dulbecco's Modified Eagle Medium (DMEM, Gibco) supplemented with 4.5 mg/ml glucose and 10% (v/v) fetal bovine serum (FBS, Gibco), were co-transfected with the expression plasmids for $\text{Na}_v1.4$, with or without $\beta 1$, and an eGFP-encoding plasmid when cell confluence reached 50%. After incubation at 37°C under 5% CO₂ for 24–48 hours, the cells were treated

with 0.05% trypsin (Gibco) and transferred to poly-D-lysine (Sigma)-coated 10 mm cover slips for electrophysiological characterizations.

Sodium currents were recorded using Axon 200B amplifier with Clampex10.6 software and glass micropipettes (3–4 M Ω) in HEK293T cells. For recording the voltage-dependent currents as well as the activation and inactivation currents, the electrodes were filled with the internal solution composed of (in mM) 40 CsCl, 10 NaCl, 10 EGTA, 10 HEPES, 105 CsF, pH 7.3 with CsOH. The extracellular solution contained (in mM) 130 NaCl, 4 KCl, 1 MgCl₂, 1.5 CaCl₂, 5 D-Glucose monohydrate, 5 HEPES, pH = 7.4 with NaOH. The TTX and STX inhibition currents were recorded in the same buffer with indicated concentrations of TTX and STX in the extracellular solution.

The voltage dependence of ion current was analyzed using a protocol consisting of steps from a holding potential of -90 mV to voltages ranging from -100 to 100 mV for 50 ms in 10 mV increment. In the I-V curves, the currents were normalized with the maximum and plotted against the voltage.

To measure the voltage dependence of activation, the cells were held at -90 mV, and

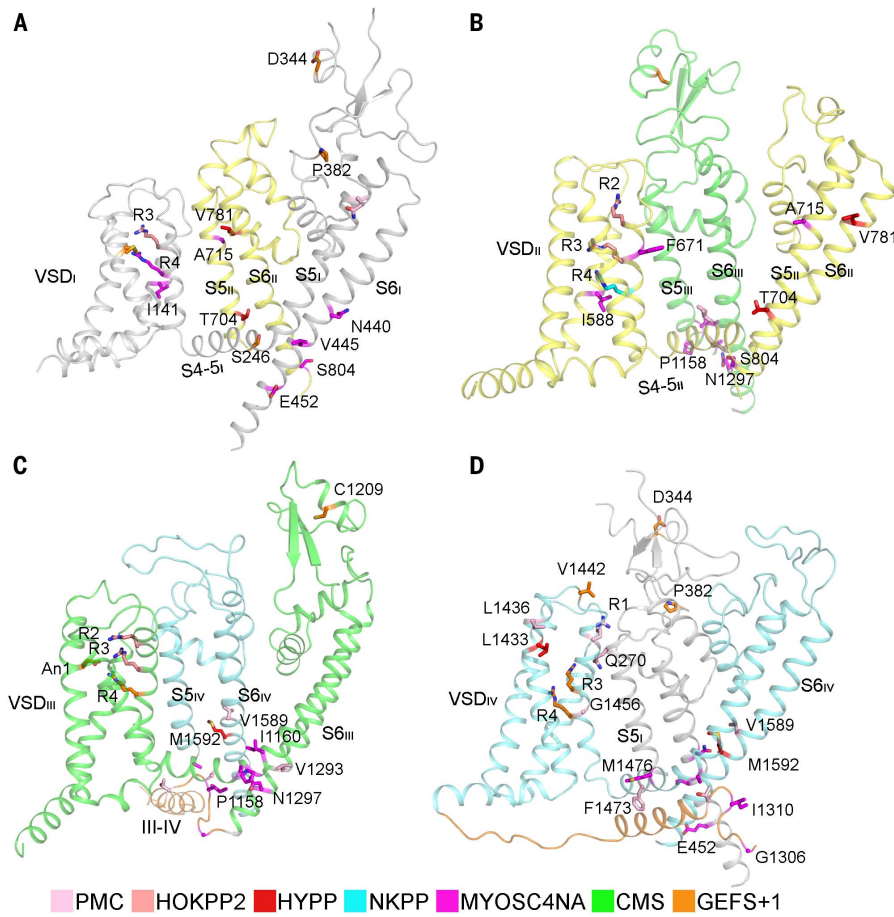


Fig. 6. Structural mapping of disease mutations in human Na_v1.4. (A to D) For better visual effect, one repeat and its interacting pore-domain elements from the adjacent repeat are shown in each panel. The disease-related residues are shown as sticks and color coded for a specific type of disease. PMC, paramyotonia congenita of von Eulenburg; HOKPP2, periodic paralysis hypokalemic 2; HYPP, periodic paralysis hyperkalemic; NKPP, normokalemic periodic paralysis; MYOSEN4A, myotonia SCN4A-related; CMS, myasthenic syndrome, congenital; GEFS+1, generalized epilepsy with febrile seizures plus 1. Details of the disease-associated mutations are presented in table S2.

pre-pulsed at -120 mV for 200 ms. Sodium current was elicited by a stepped depolarization test voltage pulsed from -80 mV to 80 mV for 50 ms with an increment of 5 mV. For the conductance calculation, the equation, $G = I/(V - V_r)$, where V_r (the reversal potential) represents the voltage at which the current is zero, was used. The calculated conductance was normalized and plotted against the voltage from -80 mV to 0 mV.

For the voltage dependence of inactivation, the cells were clamped at a holding potential of -90 mV, and were applied to step pre-pulses from -100 mV to 40 mV for 1000 ms with an increment of 5 mV. The sodium current was then recorded at the test pulse of 0 mV for 50 ms. The peak currents under the test pulses were normalized and plotted against the pre-pulse voltage.

Cryo-EM data acquisition

Aliquots of 3.5 μ l of freshly purified Na_v1.4- β 1 complex, concentrated to approximately 0.5 mg/ml, were placed on glow-discharged holey

carbon grids (Quantifoil Au 300 mesh, R1.2/L3). Grids were blotted for 3.5 s and flash-frozen in liquid ethane cooled by liquid nitrogen using Vitrobot Mark IV (Thermo Fisher). Prepared grids were subsequently transferred to a Titan Krios electron microscopy (Thermo Fisher) operated at 300 kV and equipped with Cs corrector, Gatan K2 Summit detector, and GIF Quantum energy filter. A total of 8,009 movie stacks were automatically collected using AutoEMation (73) with a slit width of 20 eV on the energy filter and a preset defocus range from -1.8 μ m to -1.5 μ m in super-resolution mode at a nominal magnification of 105,000 X. Each stack was exposed for 5.6 s with the exposing time of 0.175 s per frame, resulting in 32 frames per stack. The total dose rate was 48 e⁻/Å² for each stack. The stacks were motion corrected with MotionCor2 (74) and binned 2 fold, resulting in a pixel size of 1.091 Å/pixel. Meanwhile, dose weighting was performed (75). The defocus values were estimated with Gctf (76).

Image processing

A diagram of data processing is presented in fig. S3. A total of 1,714,341 particles were automatically picked using RELION (77–79) from 7,262 manually selected micrographs. 2D classification identified 580,143 good particles that were subsequently applied to global angular searching 3D classification with K set to 1 (one class). For each of the last several iterations of the global angular searching 3D classification, a local angular searching 3D classification was performed, during which the particles were classified into 4 classes. A total of 391,294 non-redundant particles were selected from the local angular searching 3D classification and subjected to 3 cycles of multi-reference 3D classification to remove bad particles. The selected particles were subjected to 3D auto-refinement, generating a 3D map with an overall resolution of 3.3 Å, which was further improved to 3.2 Å after local defocus correction with Gctf. The final particle number used for the 3D auto-refinement was 191,936. 2D classification, 3D classification, and auto-refinement were performed in RELION 2.1. The resolution was estimated with the gold-standard Fourier shell correlation 0.143 criterion (80) with high resolution noise substitution (81).

Model building and structure refinement

The sequences were aligned using Clustal W (82). Model building was carried out on the basis of the 3.2-Å reconstruction map. The coordinates of EeNa_v1.4- β 1 (PDB accession number: 5XSY) were fitted into the EM map by CHIMERA (83). The sequence of EeNa_v1.4- β 1 were mutated with corresponding residues in human Na_v1.4- β 1 in COOT (84) and every residue was manually examined. The chemical properties of amino acids were considered during model building.

In total 1,138 residues in Na_v1.4 and 173 residues in β 1 were assigned with side chains, and 9 sugar moieties, 6 lipid molecules, and 1 GDN were built. For Na_v1.4, the N-terminal 118 residues, extracellular loop (residues 287–335), intracellular I-II linker (residues 464–558), II-III linker (residues 807–1014), and C-terminal sequences after Glu1607 were not built due to the lack of corresponding densities.

Structure refinement was performed using phenix.real_space_refine application in PHENIX (85) in real space with secondary structure and geometry restraints. Over-fitting of the overall model was monitored by refining the model in one of the two independent maps from the gold-standard refinement approach and testing the refined model against the other map (86). Statistics of the map reconstruction and model refinement can be found in table S1.

REFERENCES AND NOTES

1. A. L. Hodgkin, A. F. Huxley, Resting and action potentials in single nerve fibres. *J. Physiol.* **104**, 176–195 (1945). doi: 10.1113/jphysiol.1945.sp004114; pmid: 16991677
2. A. L. Hodgkin, A. F. Huxley, A quantitative description of membrane current and its application to conduction and excitation in nerve. *J. Physiol.* **117**, 500–544 (1952). doi: 10.1113/jphysiol.1952.sp004764; pmid: 12991237
3. B. Hille, *Ion Channels of Excitable Membranes* (Sinauer Associates, ed. 3, 2001), pp. 814.

4. W. A. Catterall, From ionic currents to molecular mechanisms: The structure and function of voltage-gated sodium channels. *Neuron* **26**, 13–25 (2000). doi: [10.1016/S0896-6273\(00\)81133-2](https://doi.org/10.1016/S0896-6273(00)81133-2); pmid: [10798388](https://pubmed.ncbi.nlm.nih.gov/10798388/)
5. C. A. Ahern, J. Payandeh, F. Bosmans, B. Chanda, The hitchhiker's guide to the voltage-gated sodium channel galaxy. *J. Gen. Physiol.* **147**, 1–24 (2016). doi: [10.1085/jgp.201511492](https://doi.org/10.1085/jgp.201511492); pmid: [26712848](https://pubmed.ncbi.nlm.nih.gov/26712848/)
6. C. J. Woolf, R. J. Mannion, Neuropathic pain: Aetiology, symptoms, mechanisms, and management. *Lancet* **353**, 1959–1964 (1999). doi: [10.1016/S0140-6736\(99\)01307-0](https://doi.org/10.1016/S0140-6736(99)01307-0); pmid: [10371588](https://pubmed.ncbi.nlm.nih.gov/10371588/)
7. W. A. Catterall, Sodium channels, inherited epilepsy, and antiepileptic drugs. *Annu. Rev. Pharmacol. Toxicol.* **54**, 317–338 (2014). doi: [10.1146/annurev-pharmtox-011112-140232](https://doi.org/10.1146/annurev-pharmtox-011112-140232); pmid: [24392695](https://pubmed.ncbi.nlm.nih.gov/24392695/)
8. W. Huang, M. Liu, S. F. Yan, N. Yan, Structure-based assessment of disease-related mutations in human voltage-gated sodium channels. *Protein Cell* **8**, 401–438 (2017). doi: [10.1007/s13238-017-0372-z](https://doi.org/10.1007/s13238-017-0372-z); pmid: [28150151](https://pubmed.ncbi.nlm.nih.gov/28150151/)
9. M. Rubinstein et al., Association of rare missense variants in the second intracellular loop of $\text{Na}_V1.7$ sodium channels with familial autism. *Mol. Psychiatry* **23**, 231–239 (2018). doi: [10.1038/mp.2016.222](https://doi.org/10.1038/mp.2016.222); pmid: [27956748](https://pubmed.ncbi.nlm.nih.gov/27956748/)
10. W. A. Catterall et al., Voltage-gated ion channels and gating modifier toxins. *Toxicol.* **49**, 124–141 (2007). doi: [10.1016/j.toxicon.2006.09.022](https://doi.org/10.1016/j.toxicon.2006.09.022); pmid: [17239913](https://pubmed.ncbi.nlm.nih.gov/17239913/)
11. S. K. Bagal, B. E. Marron, R. M. Owen, R. I. Storer, N. A. Swain, Voltage gated sodium channels as drug discovery targets. *Channels* **9**, 360–366 (2015). doi: [10.1080/19336950.2015.1079674](https://doi.org/10.1080/19336950.2015.1079674); pmid: [26646477](https://pubmed.ncbi.nlm.nih.gov/26646477/)
12. M. R. Israel, B. Tay, J. R. Deuis, I. Vetter, Sodium channels and venom peptide pharmacology. *Adv. Pharmacol.* **79**, 67–116 (2017). doi: [10.1016/bsa.apha.2017.01.004](https://doi.org/10.1016/bsa.apha.2017.01.004); pmid: [28528674](https://pubmed.ncbi.nlm.nih.gov/28528674/)
13. W. A. Catterall, A. L. Goldin, S. G. Waxman, International Union of Pharmacology. XLVII. Nomenclature and structure-function relationships of voltage-gated sodium channels. *Pharmacol. Rev.* **57**, 397–409 (2005). doi: [10.1124/pr.57.4.4](https://doi.org/10.1124/pr.57.4.4); pmid: [16382098](https://pubmed.ncbi.nlm.nih.gov/16382098/)
14. H. A. O'Malley, L. L. Isom, Sodium channel β subunits: Emerging targets in channelopathies. *Annu. Rev. Physiol.* **77**, 481–504 (2015). doi: [10.1146/annurev-physiol-021014-071846](https://doi.org/10.1146/annurev-physiol-021014-071846); pmid: [25668026](https://pubmed.ncbi.nlm.nih.gov/25668026/)
15. F. H. Yu, V. Yarov-Yarovoy, G. A. Gutman, W. A. Catterall, Overview of molecular relationships in the voltage-gated ion channel superfamily. *Pharmacol. Rev.* **57**, 387–395 (2005). doi: [10.1124/pr.57.4.13](https://doi.org/10.1124/pr.57.4.13); pmid: [16382097](https://pubmed.ncbi.nlm.nih.gov/16382097/)
16. M. Noda et al., Primary structure of *Electrophorus electricus* sodium channel deduced from cDNA sequence. *Nature* **312**, 121–127 (1984). doi: [10.1038/312121a0](https://doi.org/10.1038/312121a0); pmid: [6209577](https://pubmed.ncbi.nlm.nih.gov/6209577/)
17. H. Terlau et al., Mapping the site of block by tetrodotoxin and saxitoxin of sodium channel II. *FEBS Lett.* **293**, 93–96 (1991). doi: [10.1016/0014-5793\(91\)81159-6](https://doi.org/10.1016/0014-5793(91)81159-6); pmid: [1660007](https://pubmed.ncbi.nlm.nih.gov/1660007/)
18. I. Favre, E. Moczydlowski, L. Schild, On the structural basis for ionic selectivity among Na^+ , K^+ , and Ca^{2+} in the voltage-gated sodium channel. *Biophys. J.* **71**, 3110–3125 (1996). doi: [10.1016/S0006-3495\(96\)79505-X](https://doi.org/10.1016/S0006-3495(96)79505-X); pmid: [8968582](https://pubmed.ncbi.nlm.nih.gov/8968582/)
19. R. W. Aldrich, D. P. Corey, C. F. Stevens, A reinterpretation of mammalian sodium channel gating based on single channel recording. *Nature* **306**, 436–441 (1983). doi: [10.1038/306436a0](https://doi.org/10.1038/306436a0); pmid: [6316158](https://pubmed.ncbi.nlm.nih.gov/6316158/)
20. C. M. Armstrong, F. Bezanilla, Currents related to movement of the gating particles of the sodium channels. *Nature* **242**, 459–461 (1973). doi: [10.1038/242459a0](https://doi.org/10.1038/242459a0); pmid: [4700900](https://pubmed.ncbi.nlm.nih.gov/4700900/)
21. C. M. Armstrong, F. Bezanilla, Charge movement associated with the opening and closing of the activation gates of the Na channels. *J. Gen. Physiol.* **63**, 533–552 (1974). doi: [10.1085/jgp.63.5.533](https://doi.org/10.1085/jgp.63.5.533); pmid: [4824995](https://pubmed.ncbi.nlm.nih.gov/4824995/)
22. N. Yang, R. Horn, Evidence for voltage-dependent S4 movement in sodium channels. *Neuron* **15**, 213–218 (1995). doi: [10.1016/0896-6273\(95\)90078-0](https://doi.org/10.1016/0896-6273(95)90078-0); pmid: [7619524](https://pubmed.ncbi.nlm.nih.gov/7619524/)
23. N. Yang, A. L. George Jr., R. Horn, Molecular basis of charge movement in voltage-gated sodium channels. *Neuron* **16**, 113–122 (1996). doi: [10.1016/S0896-6273\(00\)80028-8](https://doi.org/10.1016/S0896-6273(00)80028-8); pmid: [8562074](https://pubmed.ncbi.nlm.nih.gov/8562074/)
24. C. Miller, Biophysics. Lonely voltage sensor seeks protons for permeation. *Science* **312**, 534–535 (2006). doi: [10.1126/science.1171786](https://doi.org/10.1126/science.1171786); pmid: [16645081](https://pubmed.ncbi.nlm.nih.gov/16645081/)
25. C. M. Armstrong, F. Bezanilla, E. Rojas, Destruction of sodium conductance inactivation in squid axons perfused with pronase. *J. Gen. Physiol.* **62**, 375–391 (1973). doi: [10.1085/jgp.62.4.375](https://doi.org/10.1085/jgp.62.4.375); pmid: [4755846](https://pubmed.ncbi.nlm.nih.gov/4755846/)
26. F. Bezanilla, C. M. Armstrong, Inactivation of the sodium channel. I. Sodium current experiments. *J. Gen. Physiol.* **70**, 549–566 (1977). doi: [10.1085/jgp.70.5.549](https://doi.org/10.1085/jgp.70.5.549); pmid: [591911](https://pubmed.ncbi.nlm.nih.gov/591911/)
27. C. M. Armstrong, F. Bezanilla, Inactivation of the sodium channel. II. Gating current experiments. *J. Gen. Physiol.* **70**, 567–590 (1977). doi: [10.1085/jgp.70.5.567](https://doi.org/10.1085/jgp.70.5.567); pmid: [591912](https://pubmed.ncbi.nlm.nih.gov/591912/)
28. D. E. Patton, J. W. West, W. A. Catterall, A. L. Goldin, Amino acid residues required for fast Na^+ -channel inactivation: Charge neutralizations and deletions in the III–IV linker. *Proc. Natl. Acad. Sci. U.S.A.* **89**, 10905–10909 (1992). doi: [10.1073/pnas.89.22.10905](https://doi.org/10.1073/pnas.89.22.10905); pmid: [1332059](https://pubmed.ncbi.nlm.nih.gov/1332059/)
29. J. W. West et al., A cluster of hydrophobic amino acid residues required for fast Na^+ -channel inactivation. *Proc. Natl. Acad. Sci. U.S.A.* **89**, 10910–10914 (1992). doi: [10.1073/pnas.89.22.10910](https://doi.org/10.1073/pnas.89.22.10910); pmid: [1332060](https://pubmed.ncbi.nlm.nih.gov/1332060/)
30. A. L. Goldin, Mechanisms of sodium channel inactivation. *Curr. Opin. Neurobiol.* **13**, 284–290 (2003). doi: [10.1016/S0959-4388\(03\)00065-5](https://doi.org/10.1016/S0959-4388(03)00065-5); pmid: [12850212](https://pubmed.ncbi.nlm.nih.gov/12850212/)
31. W. Ulbricht, Sodium channel inactivation: Molecular determinants and modulation. *Physiol. Rev.* **85**, 1271–1301 (2005). doi: [10.1152/physrev.00024.2004](https://doi.org/10.1152/physrev.00024.2004); pmid: [16183913](https://pubmed.ncbi.nlm.nih.gov/16183913/)
32. Y. Jiang et al., X-ray structure of a voltage-dependent K^+ channel. *Nature* **423**, 33–41 (2003). doi: [10.1038/nature01580](https://doi.org/10.1038/nature01580); pmid: [12721618](https://pubmed.ncbi.nlm.nih.gov/12721618/)
33. S. B. Long, E. B. Campbell, R. Mackinnon, Crystal structure of a mammalian voltage-dependent Shaker family K^+ channel. *Science* **309**, 897–903 (2005). doi: [10.1126/science.1116269](https://doi.org/10.1126/science.1116269); pmid: [16002581](https://pubmed.ncbi.nlm.nih.gov/16002581/)
34. M. Liao, E. Cao, D. Julius, Y. Cheng, Structure of the TRPV1 ion channel determined by electron cryo-microscopy. *Nature* **504**, 107–112 (2013). doi: [10.1038/nature12822](https://doi.org/10.1038/nature12822); pmid: [24305160](https://pubmed.ncbi.nlm.nih.gov/24305160/)
35. J. Wu et al., Structure of the voltage-gated calcium channel $\text{Ca}_{v}1.1$ complex. *Science* **350**, aad2395 (2015). doi: [10.1126/science.aad2395](https://doi.org/10.1126/science.aad2395); pmid: [26680202](https://pubmed.ncbi.nlm.nih.gov/26680202/)
36. H. Shen et al., Structure of a eukaryotic voltage-gated sodium channel at near-atomic resolution. *Science* **355**, eaal4326 (2017). doi: [10.1126/science.aal4326](https://doi.org/10.1126/science.aal4326); pmid: [28183995](https://pubmed.ncbi.nlm.nih.gov/28183995/)
37. Z. Yan et al., Structure of the $\text{Na}_{v}1.4\beta 1$ complex from electric eel. *Cell* **170**, 470–482.e11 (2017). doi: [10.1016/j.cell.2017.06.039](https://doi.org/10.1016/j.cell.2017.06.039); pmid: [28735751](https://pubmed.ncbi.nlm.nih.gov/28735751/)
38. Y. He, K. Wang, N. Yan, The recombinant expression systems for structure determination of eukaryotic membrane proteins. *Protein Cell* **5**, 658–672 (2014). doi: [10.1007/s13238-014-0086-4](https://doi.org/10.1007/s13238-014-0086-4); pmid: [25119489](https://pubmed.ncbi.nlm.nih.gov/25119489/)
39. J. S. Trimmer et al., Primary structure and functional expression of a mammalian skeletal muscle sodium channel. *Neuron* **3**, 33–49 (1989). doi: [10.1016/0896-6273\(89\)90113-X](https://doi.org/10.1016/0896-6273(89)90113-X); pmid: [2559760](https://pubmed.ncbi.nlm.nih.gov/2559760/)
40. A. L. George Jr., J. Komisaroff, R. G. Kallen, R. L. Barchi, Primary structure of the adult human skeletal muscle voltage-dependent sodium channel. *Ann. Neurol.* **31**, 131–137 (1992). doi: [10.1002/ana.410310203](https://doi.org/10.1002/ana.410310203); pmid: [1315496](https://pubmed.ncbi.nlm.nih.gov/1315496/)
41. M. Chahine, P. B. Bennett, A. L. George Jr., R. Horn, Functional expression and properties of the human skeletal muscle sodium channel. *Pflügers Arch.* **427**, 136–142 (1994). doi: [10.1007/BF00585952](https://doi.org/10.1007/BF00585952); pmid: [8058462](https://pubmed.ncbi.nlm.nih.gov/8058462/)
42. B. Chanda, F. Bezanilla, Tracking voltage-dependent conformational changes in skeletal muscle sodium channel during activation. *J. Gen. Physiol.* **120**, 629–645 (2002). doi: [10.1085/jgp.20028679](https://doi.org/10.1085/jgp.20028679); pmid: [12407076](https://pubmed.ncbi.nlm.nih.gov/12407076/)
43. Y. Muroi, M. Arcisio-Miranda, S. Chowdhury, B. Chanda, Molecular determinants of coupling between the domain III voltage sensor and pore of a sodium channel. *Nat. Struct. Mol. Biol.* **17**, 230–237 (2010). doi: [10.1038/nsmb.1749](https://doi.org/10.1038/nsmb.1749); pmid: [2018934](https://pubmed.ncbi.nlm.nih.gov/2018934/)
44. S. Sokolov, T. Scheuer, W. A. Catterall, Ion permeation and block of the gating pore in the voltage sensor of $\text{Na}_{v}1.4$ channels with hypokalemic periodic paralysis mutations. *J. Gen. Physiol.* **136**, 225–236 (2010). doi: [10.1085/jgp.201010414](https://doi.org/10.1085/jgp.201010414); pmid: [20660662](https://pubmed.ncbi.nlm.nih.gov/20660662/)
45. P. Gosselin-Badarouline, L. Delemotte, A. Moreau, M. L. Klein, M. Chahine, Gating pore currents and the resting state of $\text{Na}_{v}1.4$ voltage sensor domains. *Proc. Natl. Acad. Sci. U.S.A.* **109**, 19250–19255 (2012). doi: [10.1073/pnas.1217990109](https://doi.org/10.1073/pnas.1217990109); pmid: [23134726](https://pubmed.ncbi.nlm.nih.gov/23134726/)
46. T. Kubota et al., Mapping of voltage sensor positions in resting and inactivated mammalian sodium channels by LRET. *Proc. Natl. Acad. Sci. U.S.A.* **114**, E1857–E1865 (2017). doi: [10.1073/pnas.1700453114](https://doi.org/10.1073/pnas.1700453114); pmid: [28202723](https://pubmed.ncbi.nlm.nih.gov/28202723/)
47. X.-W. Dong, T. Priestley, Electrophysiological analysis of tetrodotoxin-resistant sodium channel pharmacology. *Curr. Protoc. Pharmacol.* **23**, 11.8.1–11.8.33 (2004). doi: [10.1002/04711475.ph1108s23](https://doi.org/10.1002/04711475.ph1108s23); pmid: [21956811](https://pubmed.ncbi.nlm.nih.gov/21956811/)
48. J. Webb, F.-f. Wu, S. C. Cannon, Slow inactivation of the $\text{NaV}1.4$ sodium channel in mammalian cells is impeded by co-expression of the $\beta 1$ subunit. *Pflügers Arch.* **457**, 1253–1263 (2009). doi: [10.1007/s00424-008-0600-8](https://doi.org/10.1007/s00424-008-0600-8); pmid: [18941776](https://pubmed.ncbi.nlm.nih.gov/18941776/)
49. A. Goehring et al., Screening and large-scale expression of membrane proteins in mammalian cells for structural studies. *Nat. Protoc.* **9**, 2574–2585 (2014). doi: [10.1038/nprot.2014.173](https://doi.org/10.1038/nprot.2014.173); pmid: [25299155](https://pubmed.ncbi.nlm.nih.gov/25299155/)
50. B. Hille, The permeability of the sodium channel to metal cations in myelinated nerve. *J. Gen. Physiol.* **59**, 637–658 (1972). doi: [10.1085/jgp.59.6.637](https://doi.org/10.1085/jgp.59.6.637); pmid: [5025743](https://pubmed.ncbi.nlm.nih.gov/5025743/)
51. H. Shen et al., Structural basis for the modulation of voltage-gated sodium channels by animal toxins. *Science* **2018**, eaau2596 (2018). doi: [10.1126/science.aau2596](https://doi.org/10.1126/science.aau2596); pmid: [30049784](https://pubmed.ncbi.nlm.nih.gov/30049784/)
52. B. Hille, The permeability of the sodium channel to organic cations in myelinated nerve. *J. Gen. Physiol.* **58**, 599–619 (1971). doi: [10.1085/jgp.58.6.599](https://doi.org/10.1085/jgp.58.6.599); pmid: [5315827](https://pubmed.ncbi.nlm.nih.gov/5315827/)
53. J. Zhang et al., Simulating the ion permeation and ion selection for a eukaryotic voltage-gated sodium channel Na_{v}PaS . *Protein Cell* **9**, 580–585 (2018). doi: [10.1007/s13238-018-0522-y](https://doi.org/10.1007/s13238-018-0522-y); pmid: [29532417](https://pubmed.ncbi.nlm.nih.gov/29532417/)
54. C. M. Armstrong, Sodium channels and gating currents. *Physiol. Rev.* **61**, 644–683 (1981). doi: [10.1152/physrev.1981.61.3.644](https://doi.org/10.1152/physrev.1981.61.3.644); pmid: [6265962](https://pubmed.ncbi.nlm.nih.gov/6265962/)
55. P. G. DeCaen, V. Yarov-Yarovoy, Y. Zhao, T. Scheuer, W. A. Catterall, Disulfide locking a sodium channel voltage sensor reveals ion pair formation during activation. *Proc. Natl. Acad. Sci. U.S.A.* **105**, 15142–15147 (2008). doi: [10.1073/pnas.0806486105](https://doi.org/10.1073/pnas.0806486105); pmid: [18809926](https://pubmed.ncbi.nlm.nih.gov/18809926/)
56. P. G. DeCaen, V. Yarov-Yarovoy, E. M. Sharp, T. Scheuer, W. A. Catterall, Sequential formation of ion pairs during activation of a sodium channel voltage sensor. *Proc. Natl. Acad. Sci. U.S.A.* **106**, 22498–22503 (2009). doi: [10.1073/pnas.0912307106](https://doi.org/10.1073/pnas.0912307106); pmid: [20007787](https://pubmed.ncbi.nlm.nih.gov/20007787/)
57. X. Zhang et al., Crystal structure of an orthologue of the NaChBac voltage-gated sodium channel. *Nature* **486**, 130–134 (2012). doi: [10.1038/nature1054](https://doi.org/10.1038/nature1054); pmid: [22678295](https://pubmed.ncbi.nlm.nih.gov/22678295/)
58. X. Tao, A. Lee, W. Limapichat, D. A. Dougherty, R. Mackinnon, A gating charge transfer center voltage sensors. *Science* **328**, 67–73 (2010). doi: [10.1126/science.1185954](https://doi.org/10.1126/science.1185954); pmid: [20360102](https://pubmed.ncbi.nlm.nih.gov/20360102/)
59. J. Wu et al., Structure of the voltage-gated calcium channel $\text{Ca}_{v}1.1$ at 3.6 Å resolution. *Nature* **537**, 191–196 (2016). doi: [10.1038/nature19321](https://doi.org/10.1038/nature19321); pmid: [27580036](https://pubmed.ncbi.nlm.nih.gov/27580036/)
60. M. P. Goldschien-Ohm, D. L. Capes, K. M. Oelstrom, B. Chanda, Multiple pore conformations driven by asynchronous movements of voltage sensors in a eukaryotic sodium channel. *Nat. Commun.* **4**, 1350 (2013). doi: [10.1038/ncomms2356](https://doi.org/10.1038/ncomms2356); pmid: [23322038](https://pubmed.ncbi.nlm.nih.gov/23322038/)
61. H. K. Motoike et al., The Na^+ channel inactivation gate is a molecular complex: A novel role of the COOH-terminal domain. *J. Gen. Physiol.* **123**, 155–165 (2004). doi: [10.1085/jgp.200308929](https://doi.org/10.1085/jgp.200308929); pmid: [14744988](https://pubmed.ncbi.nlm.nih.gov/14744988/)
62. R. S. Kass, Sodium channel inactivation goes with the flow. *J. Gen. Physiol.* **124**, 7–8 (2004). doi: [10.1085/jgp.200409123](https://doi.org/10.1085/jgp.200409123); pmid: [15226362](https://pubmed.ncbi.nlm.nih.gov/15226362/)
63. R. S. Kass, Sodium channel inactivation in heart: A novel role of the carboxy-terminal domain. *J. Cardiovasc. Electrophysiol.* **17** (suppl. 1), S21–S25 (2006). doi: [10.1111/j.1540-8167.2006.00381.x](https://doi.org/10.1111/j.1540-8167.2006.00381.x); pmid: [16686678](https://pubmed.ncbi.nlm.nih.gov/16686678/)
64. L. Tang, R. G. Kallen, R. Horn, Role of an S4–S5 linker in sodium channel inactivation probed by mutagenesis and a peptide blocker. *J. Gen. Physiol.* **108**, 89–104 (1996). doi: [10.1085/jgp.108.2.89](https://doi.org/10.1085/jgp.108.2.89); pmid: [8854339](https://pubmed.ncbi.nlm.nih.gov/8854339/)
65. J. C. McPhee, D. S. Ragsdale, T. Scheuer, W. A. Catterall, A critical role for the S4–S5 intracellular loop in domain IV of the sodium channel α -subunit in fast inactivation. *J. Biol. Chem.* **273**, 1121–1129 (1998). doi: [10.1074/jbc.273.2.1121](https://doi.org/10.1074/jbc.273.2.1121); pmid: [9422778](https://pubmed.ncbi.nlm.nih.gov/9422778/)
66. M. R. Smith, A. L. Goldin, Interaction between the sodium channel inactivation linker and domain III S4–S5. *Biophys. J.* **73**, 1885–1895 (1997). doi: [10.1016/S0006-3495\(97\)78219-5](https://doi.org/10.1016/S0006-3495(97)78219-5); pmid: [9336184](https://pubmed.ncbi.nlm.nih.gov/9336184/)
67. M. Bouhours et al., A1152D mutation of the Na^+ channel causes paramyotonia congenita and emphasizes the role of DIII–S4–S5 linker in fast inactivation. *J. Physiol.* **565**, 415–427 (2005). doi: [10.1113/jphysiol.2004.081018](https://doi.org/10.1113/jphysiol.2004.081018); pmid: [15790667](https://pubmed.ncbi.nlm.nih.gov/15790667/)
68. A. I. McClatchey et al., Temperature-sensitive mutations in the III–IV cytoplasmic loop region of the skeletal muscle sodium channel gene in paramyotonia congenita. *Cell* **68**, 769–774 (1992). doi: [10.1016/0092-8674\(92\)90151-2](https://doi.org/10.1016/0092-8674(92)90151-2); pmid: [1310898](https://pubmed.ncbi.nlm.nih.gov/1310898/)

69. H. Lerche *et al.*, Human sodium channel myotonia: Slowed channel inactivation due to substitutions for a glycine within the III-IV linker. *J. Physiol.* **470**, 13–22 (1993). doi: [10.1113/jphysiol.1993.sp019843](https://doi.org/10.1113/jphysiol.1993.sp019843); pmid: [8308722](https://pubmed.ncbi.nlm.nih.gov/8308722/)
70. L. J. Hayward, R. H. Brown Jr., S. C. Cannon, Inactivation defects caused by myotonia-associated mutations in the sodium channel III-IV linker. *J. Gen. Physiol.* **107**, 559–576 (1996). doi: [10.1085/jgp.107.5.559](https://doi.org/10.1085/jgp.107.5.559); pmid: [8740371](https://pubmed.ncbi.nlm.nih.gov/8740371/)
71. B. G. H. Schoser, J. M. Schröder, T. Grimm, D. Sternberg, W. Kress, A large German kindred with cold-aggravated myotonia and a heterozygous A1481D mutation in the SCN4A gene. *Muscle Nerve* **35**, 599–606 (2007). doi: [10.1002/mus.20733](https://doi.org/10.1002/mus.20733); pmid: [17212350](https://pubmed.ncbi.nlm.nih.gov/17212350/)
72. T. Matsuda, C. L. Cepko, Electroporation and RNA interference in the rodent retina *in vivo* and *in vitro*. *Proc. Natl. Acad. Sci. U.S.A.* **101**, 16–22 (2004). doi: [10.1073/pnas.2235688100](https://doi.org/10.1073/pnas.2235688100); pmid: [14603031](https://pubmed.ncbi.nlm.nih.gov/14603031/)
73. J. Lei, J. Frank, Automated acquisition of cryo-electron micrographs for single particle reconstruction on an FEI Tecnai electron microscope. *J. Struct. Biol.* **150**, 69–80 (2005). doi: [10.1016/j.jsb.2005.01.002](https://doi.org/10.1016/j.jsb.2005.01.002); pmid: [15797731](https://pubmed.ncbi.nlm.nih.gov/15797731/)
74. S. Q. Zheng *et al.*, MotionCor2: Anisotropic correction of beam-induced motion for improved cryo-electron microscopy. *Nat. Methods* **14**, 331–332 (2017). doi: [10.1038/nmeth.4193](https://doi.org/10.1038/nmeth.4193); pmid: [28250466](https://pubmed.ncbi.nlm.nih.gov/28250466/)
75. T. Grant, N. Grigorieff, Measuring the optimal exposure for single particle cryo-EM using a 2.6 Å reconstruction of rotavirus VP6. *eLife* **4**, e06980 (2015). doi: [10.7554/elife.06980](https://doi.org/10.7554/elife.06980); pmid: [26023829](https://pubmed.ncbi.nlm.nih.gov/26023829/)
76. K. Zhang, Gctf: Real-time CTF determination and correction. *J. Struct. Biol.* **193**, 1–12 (2016). doi: [10.1016/j.jsb.2015.11.003](https://doi.org/10.1016/j.jsb.2015.11.003); pmid: [26592709](https://pubmed.ncbi.nlm.nih.gov/26592709/)
77. S. H. W. Scheres, RELION: Implementation of a Bayesian approach to cryo-EM structure determination. *J. Struct. Biol.* **180**, 519–530 (2012). doi: [10.1016/j.jsb.2012.09.006](https://doi.org/10.1016/j.jsb.2012.09.006); pmid: [23000701](https://pubmed.ncbi.nlm.nih.gov/23000701/)
78. S. H. W. Scheres, Semi-automated selection of cryo-EM particles in RELION-1.3. *J. Struct. Biol.* **189**, 114–122 (2015). doi: [10.1016/j.jsb.2014.11.010](https://doi.org/10.1016/j.jsb.2014.11.010); pmid: [25486611](https://pubmed.ncbi.nlm.nih.gov/25486611/)
79. D. Kimanius, B. O. Forsberg, S. H. W. Scheres, E. Lindahl, Accelerated cryo-EM structure determination with parallelisation using GPUs in RELION-2. *eLife* **5**, e18722 (2016). doi: [10.7554/eLife.18722](https://doi.org/10.7554/eLife.18722); pmid: [27845625](https://pubmed.ncbi.nlm.nih.gov/27845625/)
80. P. B. Rosenthal, R. Henderson, Optimal determination of particle orientation, absolute hand, and contrast loss in single-particle electron cryomicroscopy. *J. Mol. Biol.* **333**, 721–745 (2003). doi: [10.1016/j.jmb.2003.07.013](https://doi.org/10.1016/j.jmb.2003.07.013); pmid: [14568533](https://pubmed.ncbi.nlm.nih.gov/14568533/)
81. S. Chen *et al.*, High-resolution noise substitution to measure overfitting and validate resolution in 3D structure determination by single particle electron cryomicroscopy. *Ultramicroscopy* **135**, 24–35 (2013). doi: [10.1016/j.ultramic.2013.06.004](https://doi.org/10.1016/j.ultramic.2013.06.004); pmid: [23872039](https://pubmed.ncbi.nlm.nih.gov/23872039/)
82. M. A. Larkin *et al.*, Clustal W and Clustal X version 2.0. *Bioinformatics* **23**, 2947–2948 (2007). doi: [10.1093/bioinformatics/btm404](https://doi.org/10.1093/bioinformatics/btm404); pmid: [17846036](https://pubmed.ncbi.nlm.nih.gov/17846036/)
83. E. F. Pettersen *et al.*, UCSF Chimera—A visualization system for exploratory research and analysis. *J. Comput. Chem.* **25**, 1605–1612 (2004). doi: [10.1002/jcc.20084](https://doi.org/10.1002/jcc.20084); pmid: [15264254](https://pubmed.ncbi.nlm.nih.gov/15264254/)
84. P. Emsley, B. Lohkamp, W. G. Scott, K. Cowtan, Features and development of Coot. *Acta Crystallogr. D Biol. Crystallogr.* **66**, 486–501 (2010). doi: [10.1107/S0907444910007493](https://doi.org/10.1107/S0907444910007493); pmid: [20383002](https://pubmed.ncbi.nlm.nih.gov/20383002/)
85. P. D. Adams *et al.*, PHENIX: A comprehensive Python-based system for macromolecular structure solution. *Acta Crystallogr. D Biol. Crystallogr.* **66**, 213–221 (2010). doi: [10.1107/S0907444909052925](https://doi.org/10.1107/S0907444909052925); pmid: [20124702](https://pubmed.ncbi.nlm.nih.gov/20124702/)
86. A. Amunts *et al.*, Structure of the yeast mitochondrial large ribosomal subunit. *Science* **343**, 1485–1489 (2014). doi: [10.1126/science.1249410](https://doi.org/10.1126/science.1249410); pmid: [24675956](https://pubmed.ncbi.nlm.nih.gov/24675956/)
87. W. L. DeLano, The PyMOL Molecular Graphics System (2002); www.pymol.org.
88. O. S. Smart, J. G. Neduvelli, X. Wang, B. A. Wallace, M. S. P. Sansom, HOLE: A program for the analysis of the pore dimensions of ion channel structural models. *J. Mol. Graph.* **14**, 354–360 (1996). doi: [10.1016/S0263-7855\(97\)00009-X](https://doi.org/10.1016/S0263-7855(97)00009-X); pmid: [9195488](https://pubmed.ncbi.nlm.nih.gov/9195488/)

ACKNOWLEDGMENTS

We thank X. Li (Tsinghua University) for technical support during EM image acquisition. **Funding:** This work was funded by the National Key Basic Research (973) Program (2015CB910101 to N.Y.) and the National Key R&D Program (2016YFA0500402 to N.Y. and 2016YFA0501100 to J.L.) from Ministry of Science and Technology of China, the National Natural Science Foundation of China (projects 31621092, 31630017, and 81861138009 to N.Y.), and China Postdoctoral Science Foundation (BX201600089 to X.P.). We thank the Tsinghua University Branch of China National Center for Protein Sciences (Beijing) for providing the cryo-EM facility support. We thank the computational facility support on the cluster of Bio-Computing Platform (Tsinghua University Branch of China National Center for Protein Sciences Beijing) and the “Explorer 100” cluster system of Tsinghua National Laboratory for Information Science and Technology. N.Y. is supported by the Shirley M. Tilghman endowed professorship from Princeton University.

Author contributions: N.Y. conceived the project. X.P.,

Z.L., Q.Z., H.S., K.W., X.H., J.C., J.Z., X.Z., and J.L. performed the experiments. All authors contributed to data analysis. N.Y. wrote the manuscript. **Competing interests:** The authors declare that they have no competing interests. **Data and materials availability:** The atomic coordinates and EM map for the human Na_{1.4}-β1 complex have been deposited in the Protein Data Bank (www.rcsb.org) and EMDB (www.ebi.ac.uk/pdbe/embdb/) with accession codes 6AGF and EMD-9617, respectively.

SUPPLEMENTARY MATERIALS

www.sciencemag.org/content/362/6412/eaau2486/suppl/DC1
Figs. S1 to S8
Tables S1 and S2

22 May 2018; accepted 20 August 2018
10.1126/science.aau2486